The effect of N addition on the micro-structure and corrosion resistance of modified 6Mo super austenitic stainless steels during isothermal aging treatment

Wang, Jian; Yao, Yi; Liu, Zhiqiang; Tian, Haiyu; Chen, Chao; Chen, Lei; Gonzalez-Garcia, Yaiza; Han, Peide

DOI
10.1177/03019233241284701

Publication date
2025

Document Version
Final published version

Published in
Ironmaking and Steelmaking

Original Research Article

I·M3
Institute of Materials, Minerals & Mining

Ironmaking & Steelmaking
1–13

DOI: 10.1177/03019233241284701
journals.sagepub.com/home/ist
Sage

The effect of N addition on the micro-structure and corrosion resistance of modified 6Mo super austenitic stainless steels during isothermal aging treatment

Jian Wang[1], Yi Yao[1], Zhiqiang Liu[1], Haiyu Tian[1], Chao Chen[1], Lei Chen[2], Yaiza Gonzalez-Garcia[3] and Peide Han[1]

Abstract

In this research, three types of super austenitic stainless steel (SASS) with nitrogen levels of 0.2, 0.28, and 0.38 wt.% were developed. By maintaining a relatively high manganese content of approximately 1.5 wt.% and nickel content of around 18 wt.%, nitrogen was fully incorporated into the austenite, resulting in alloy samples designated as 0.2N, 0.3N and 0.4N. The hot-rolled plates of these alloys underwent a solution treatment at 1180°C for 30 min, followed by aging at 950°C for durations of 30 min, 2 h and 6 h, respectively. The influence of nitrogen content on phase precipitation behaviour was examined through various micro-structure characterisation techniques. The corrosion resistance of the samples was further evaluated using potentiodynamic polarisation experiments, Electrochemical impedance spectroscopy (EIS) and double loop-electrochemical potentiokinetic reactivation (DL-EPR) method. The results indicated that with an increase in nitrogen (N) addition, the quantity of σ phases decreased while and the formation of Cr_2N phases increased during the same aging period. Furthermore, at the same aging duration, the 0.3N SASS exhibited the highest pitting resistance and the lowest degree of sensitization (DOS) value compared to all other steels, attributed to the minimal precipitates present along the grain boundaries.

Keywords

super austenitic stainless steels, sigma phase, nitrogen, precipitation behaviour, intergranular corrosion, electrochemical corrosion

Received: 23 July 2024; accepted: 28 August 2024

Introduction

Super austenitic stainless steels (SASS) have excellent corrosion resistance and mechanical properties. It have been widely used in extremely harsh corrosive environments such as marine, waste gas treatment and petrochemical industry.[1–4] The SASS with different Mo content, including 904L (4 wt.%), 254SMO (6 wt.%) and 654SMO (7 wt.%), have been manufactured to meet the practical requirement.[5,6] However, due to high Cr and Mo content, the brittle intermetallic compounds are easily precipitated during the solidification and hot working process, leading to declined mechanical and corrosion properties.[7–9]

Optimising alloy composition is an effective method to regulate the micro-structure and improve the properties of stainless steel.[10–13] For instance, the increase of Cr and Mo in S32654 SASS promoted the formation of grain boundary phase and retard the intergranular corrosion (IGC) sensitivity.[14] The replacement of 2 wt.% nickel with 2 wt.% cobalt in S32654 SASS decreased the σ phases precipitation along the grain boundary.[15] After the addition of 0.016 wt.% cerium to S31254 SASS, σ phase was replaced by δ phase in the solidification micro-structure.[16] In addition, Ce was also discovered to be used in S32654 for refining the solidification structure and inhibiting the σ phases precipitation.[17] The addition

[1]College of Materials Science and Engineering, Taiyuan University of Technology, Taiyuan, China
[2]College of Mechanical and Vehicle Engineering, Taiyuan University of Technology, Taiyuan, China
[3]Department of Materials Science and Engineering, Delft University of Technology, Delft, The Netherlands

Corresponding authors:
Jian Wang, College of Materials Science and Engineering, Taiyuan University of Technology, Taiyuan 030024, China.
Email: wangjian@tyut.edu.cn

Peide Han, College of Materials Science and Engineering, Taiyuan University of Technology, Taiyuan 030024, China.
Email: hanpeide@126.com

of Ce also can transform the type of inclusions from undissolved ones to dissolved Ce-based inclusions, and improve the corrosion resistance and mechanical properties.[18,19] The increase of Nb, Mn and C and the decrease of Mo content in S31254 SASS was beneficial to the NbC precipitation, which improves the mechanical and corrosion resistance.[20] Cu was considered to promote the formation of the main oxides Cr_2O_3 and Mo^{4+} in the inner passive film of S31254 SASS, thus improving corrosion resistance.[21] B was more prone to segregate to grain boundaries, inhibiting the diffusion of Mo, so it positively affected the inhibition of grain boundary phase precipitation at sensitive temperatures in S31254 SASS.[22,23]

Nitrogen also played a significant role in strengthening the austenite stability, and the ability of nitrogen to form austenite is about 30 times compared with Ni.[24–26] SASS is a kind of high N austenitic stainless steel. Nitrogen can stabilise the austenitic phase, delay intermetallic compound precipitation and improve mechanical and hot working properties.[27–29] The typical 6Mo SASS, including 254SMO (20Cr-18Ni-6Mo-0.7Cu-0.2N), AL-6XN (20Cr-20Ni-6.3Mo-0.22N) and NAS 224N(23Cr-22Ni-6Mo-0.25N), has been developed in the past decades.[30–32] The content of alloy elements significantly affected the solubility of N in SASS. By increasing the content of Mn and Mo, while reducing the content of Ni and Cr, the N content can be increased. Moreover, Mn has a greater impact on the solubility of N than Mo.[33] It has been reported that increasing N content in S32654 SASS containing 7 wt.% Mo is beneficial to inhibit the formation of intragranular σ phase, but accelerate the generation of Cr_2N phases.[34] However, the effect of N on the phase precipitation of 6Mo SASS has not been systematically researched.

Additionally, some researchers investigated the phenomenon that the deleterious secondary phases such as σ or Cr_2N phases is easily precipitated in grain boundary of super stainless steels with high N content.[34–38] Both the Cr-depleted and Mo-depleted zones around the σ phase and Cr-depleted zone adjacent to the Cr_2N phase were observed in different stainless steel after aging treatment, including hyper-duplex 2707 stainless steel,[35] super duplex stainless steel SAF2906[36] and lean duplex 2404 stainless steel,[37] which leads to the intergranular corrosion. As for the SASS steels, the σ phase or Cr_2N phase also precipitated and caused intergranular corrosion in S32654 SASS, and their precipitation amount depends on the added N content.[34] Previous investigation suggests that the increase of Ni content induced Mo clustering in σ phase, but the much more Mn content had the opposite effect for Mo activity.[38] However, nevertheless, there is limited information available on how nitrogen content affects the precipitation behaviour of 6Mo SASS, and the corrosion mechanisms associated with the σ and Cr_2N phases that precipitate in 6Mo SASS steel are not yet completely understood.

In this work, the impact of nitrogen on the precipitation behaviour and corrosion resistance of 6Mo SASS at 950°C has been investigated for the first time. The composition and fabrication of 6Mo SASS are meticulously controlled to create samples with nitrogen contents of 0.20, 0.28 and 0.38 wt.%, a relatively high Mn content of approximately 1.5 wt.%, and a consistent nickel content of around 18 wt.%. This is done to ensure that nitrogen is completely dissolved in the austenite and to inhibit the formation of the σ phase. The precipitation behaviour was analysed through various micro-structural characterisations. The influence of nitrogen on corrosion resistance was examined using potentiodynamic polarisation, electrochemical impedance spectroscopy analysis and the DL-EPR method. Additionally, the mechanism by which nitrogen affects the alloy's corrosion resistance was explored through phase diagram and line scanning analysis, establishing a link between corrosion behaviour and the precipitation process.

Materials and experimental procedures

Processing of the specimens

The 6Mo SASS ingots with different N content recorded as 0.2N, 0.3N and 0.4N were prepared by a 25 kg vacuum induction-melting furnace under nitrogen atmosphere, and the chemical composition of samples were measured by inductively coupled plasma mass spectrometry (ICP-MS) and shown in Table 1, respectively. The ingot was subsequently homogenised at 1250°C for 12 h and hot-rolled into 5 mm thick plate. After that, it is cut to a 15 mm×15 mm × 3 mm square block by a wire cutting machine and quickly quenched in water after solid–solution treatment at 1180°C for 30 min. For the aging treatment, all samples were further sensitised at 950°C for 30 min, 2 h and 6 h, respectively.

Micro-structure characterisation

All samples were grinded with SiC papers step by step to 2500 grit, polished like a mirror, cleaned with ethanol and distilled water in an ultrasonic bath, and etched with aqua regia for observation. The micro-structure is characterised by Leica, DM 6 M optical microscopy (OM) and EVO18 scanning electron microscope (SEM), and the elemental distributions were tested by a SHIMADZU electron probe micro-analyser (EPMA). The number and size of precipitates were counted by Image Pro Plus (IPP) software. A JEOL

Table 1. The chemical composition of 0.2N, 0.3N and 0.4N steels (mass fraction, %).

Number	C	Si	Mn	P	S	Cr	Ni	Mo	Cu	B	N	Fe
0.2N	0.019	0.59	1.55	0.009	0.005	19.88	18.69	6.14	1.02	0.004	0.20	Bal.
0.3N	0.014	0.62	1.58	0.006	0.005	20.12	18.61	6.11	0.99	0.004	0.28	Bal.
0.4N	0.013	0.54	1.56	0.007	0.004	20.34	18.89	6.14	0.98	0.004	0.38	Bal.

2100F field emission transmission electron microscope (TEM) with a Super-X energy-dispersive X-ray spectroscopy (EDS) system is further employed to analyse the microstructure. The specific TEM foils were prepared by a focused ion beam (FIB) milling technique. Thermodynamic calculations were carried out using Thermo-Calc software to predict the mass fraction of alloy elements dissolved in the alloy as a function of the temperature.

Electrochemical experiments

The electrochemical measurement was carried out in a typical three-electrode cell on a CS350 electrochemical workstation (Wuhan, China) at room temperature. The cell consisted of the specimens with an exposed area of 1 cm^2, a platinum foil and a saturated calomel (SCE) as the working, counter and reference electrodes, respectively.

EIS and potentiodynamic polarisation experiments were carried out in a 3.5% NaCl solution with a pH of 1. The open-circuit potential (OCP) was measured at 1800s. The EIS experiment frequency was set to 10^5 to 10^{-2} Hz, and the experiment results were analysed by Zview software (3.0a Scribner Associates, Inc., Southern Pines, NC, USA) and the fitting parameters were obtained. The scanning range of potentiodynamic polarisation is −0.8 to 1.5 V (relative open circuit), and the scanning frequency is 1.667 mV/s. The corrosion parameters are obtained by Tafel extrapolation method. The DL-EPR measurement was carried out in a mixed solution of 0.01 M KSCN, 2 M H_2SO_4 and 2 M HCl at room temperature. The potential at 1.667 mV/s scanning rate was applied from OCP to 200 mV and hold for 2 min, and cathodically back to OCP. The activation peak current (I_r) and activation peak current (I_a) were recorded for the calculation of DOS (DOS $/\% = 100 \times I_r/I_a$). All experimental experiments were repletely for three times for reproducibility.

Results and discussion

Phase precipitation in 6Mo SASS with different N content after aging treatment

SEM characterisation. Figure 1 shows the micro-structure of the solid–solution 6Mo SASS with different N content. It is evident that all the samples have a similar grain size, with minimal precipitation occurring at the grain boundaries and within the crystals. However, as displayed in Figure 2, the examined alloys with different N content levels display notable differences in the amount and distribution of precipitates following sensitisation treatment. For the 0.2N SASS, precipitates begin to form along the grain boundaries after aging at 950°C for 30 min, and subsequently appear within the grains as aging time increases. In contrast, the 0.3N SASS shows significantly fewer precipitates than the 0.2N samples during the same aging duration, suggesting that higher N content can suppress precipitation. When the N content reaches 0.38 wt.%, the amount of precipitates at the grain boundaries and within the grains in 0.4N samples surpasses that of the 0.2N and 0.3N samples at the same aging time. The area fraction of precipitates for the three alloys at different aging durations was calculated using IPP software, with results presented in Figure 3. The area fraction of the second phase markedly increases when raising the time from 30 min to 6 h, which is attributed to the rapid growth of precipitates at grain boundaries. In addition, the area fraction of the precipitated phase in 0.3N alloy is significantly lower than that of the other two samples, demonstrating that the change of N content has a regulatory effect on the precipitated phase.

Figure 4 further shows the enlarged Scanning electron microscope-Back scattered Electron (SEM-BSE) images of the three samples aged at 950°C for various time, and the EDS of phases at the site 1 to 10 of grain boundary was measured to confirm the chemical compounds (Table 2). The light-white phases have a high Mo content of about 14.3 to 22.7 wt.% and Cr content of about 17.2 to 22.3 wt.% belongs to σ phases,[9,39] and the dark-grey phases, which contain a noticeable Cr and N content than σ phases, can be assigned to the Cr_2N phase. When aging time is at 30 min, the 0.3N alloy exhibited much less σ phases precipitated along the grain boundary than the 0.2N alloys, but more Cr_2N phases formed at the 0.4N alloys. As the aging time is prolonged to 2 h, the precipitates increased obviously at the grain boundary, and a large number of precipitates was also formed in the austenite matrix. At this point, 0.3N had the fewest secondary phases compared to 0.2N and 0.4N. The precipitation

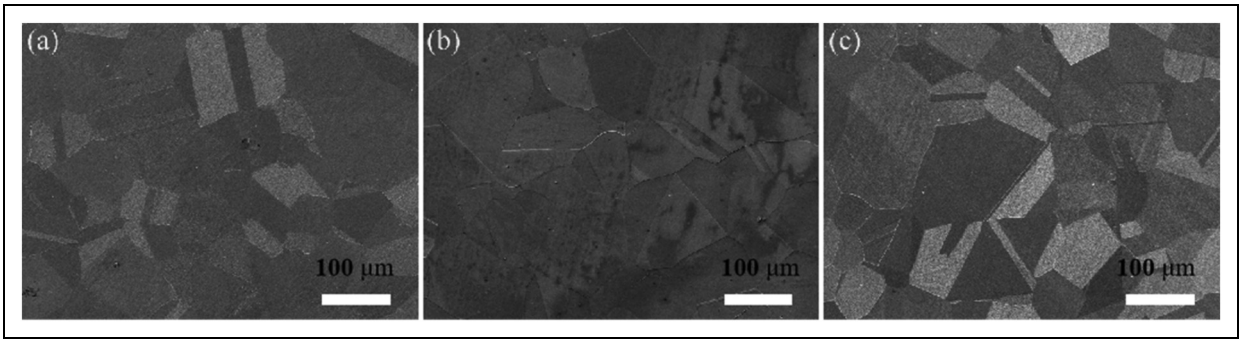

Figure 1. SEM micrographs of 6Mo SASS with various N content after solid–solution treatment, (a) 0.2N, (b) 0.3N and (c) 0.4N. SASS: super austenitic stainless steel; SEM: scanning electron microscope.

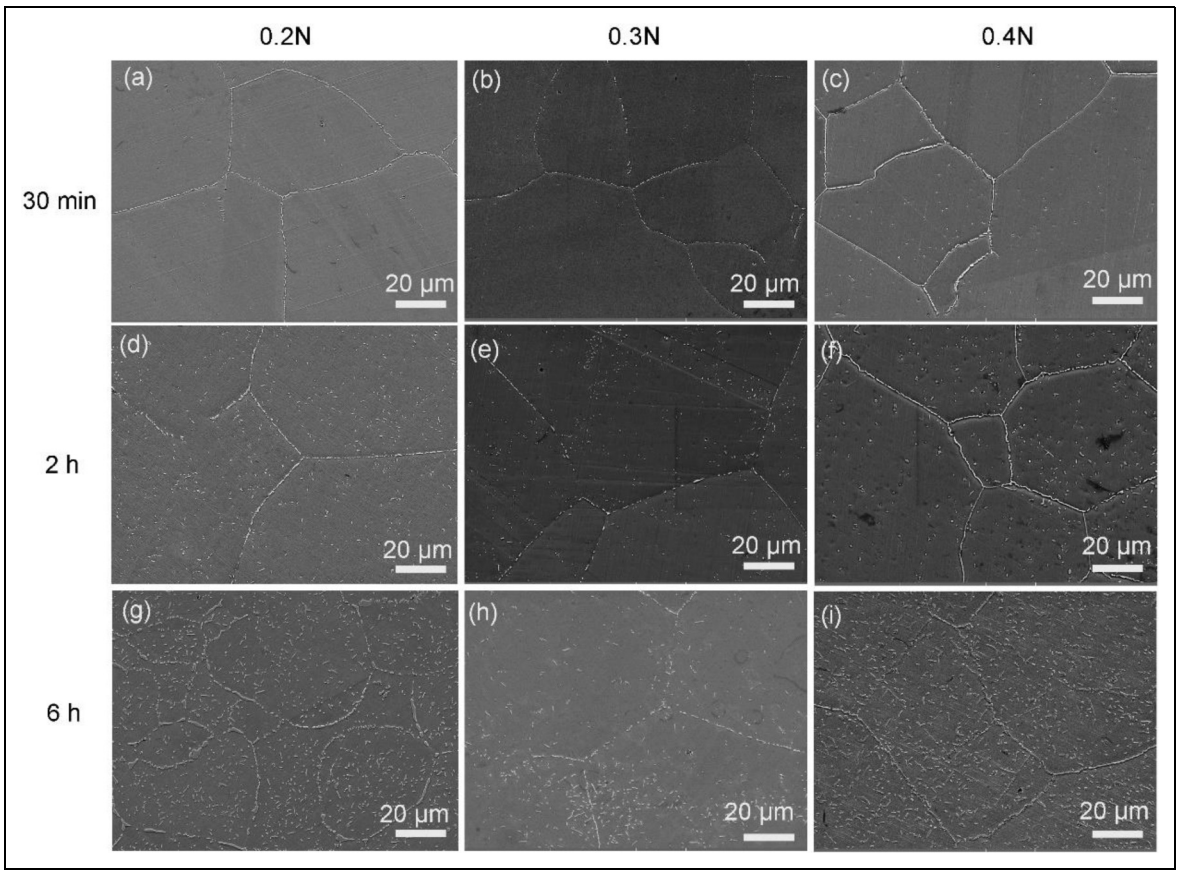

Figure 2. SEM images of the micro-structures corresponding to the samples 0.2N, 0.3N and 0.4N after aging at 950°C for 30 min ((a)–(c)), 2 h ((d)–(f)) and 6 h ((g)–(i)). SEM: scanning electron microscope.

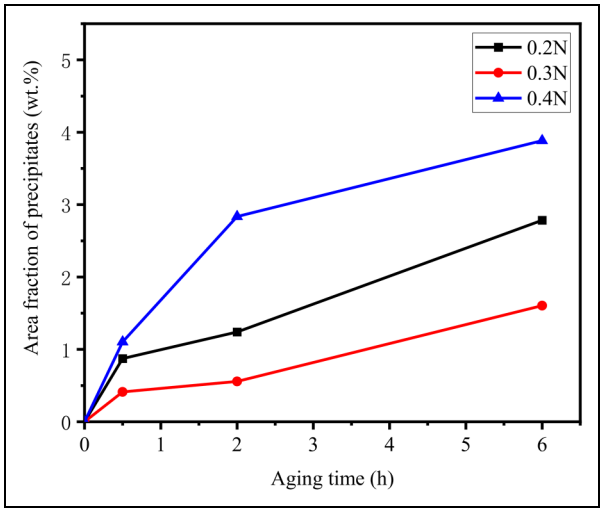

Figure 3. Statistic analysis of grain boundary precipitates amount for the samples at the different aging time.

phases of grain interior and grain boundary of the alloy further coarsen after aging for 6 h, but the Cr_2N phases almost cannot be observed in 0.2N alloys and covered the grain boundary in the 0.4N alloy.

Figure 5 shows the SEM-EDS mapping of the grain boundary precipitates in aged – 6 h 0.2N, 0.3N and 0.4N steels. Mo greatly segregated to the grain boundary of 0.2N and 0.3N steels, but other elements are poor in the boundary zone. The few N segregation in 0.2N and 0.3N 6Mo SASS indicates that most of the precipitates at the grain boundary are σ phases. However, Cr and N segregations along the grain boundary of 0.4N steels were observed, indicating the formation of Cr_2N at the grain boundary. According to earlier research,[34] both the driving force for the σ phase and the activity of the Cr element decrease in a linear manner as nitrogen content increases. Therefore, a proper rise in nitrogen levels can effectively hinder the formation of the σ phase. However, despite the reduced activity of the Cr element, nitrogen is a crucial component for the formation of the Cr_2N phase, and higher nitrogen content boosts the driving force for Cr_2N phase formation, promoting its development. As a result, while increased nitrogen content prevents the precipitation of the σ phase, it also supports the formation of the Cr_2N phase.

High-resolution TEM characterisation. Figures 6 to 8 present the TEM images and selected area electron diffraction (SAED) patterns of precipitates in the 0.2N, 0.3N and 0.4N alloys after aging for 6 h, and the chemical composition of the precipitates located site 1 to 5 which was signed in Figures 6 to 8 as outlined in Table 3. As shown in Figure 6(a) and (b), the phase in aged – 6 h 0.2N alloys was identified as σ phase with the lattice parameter

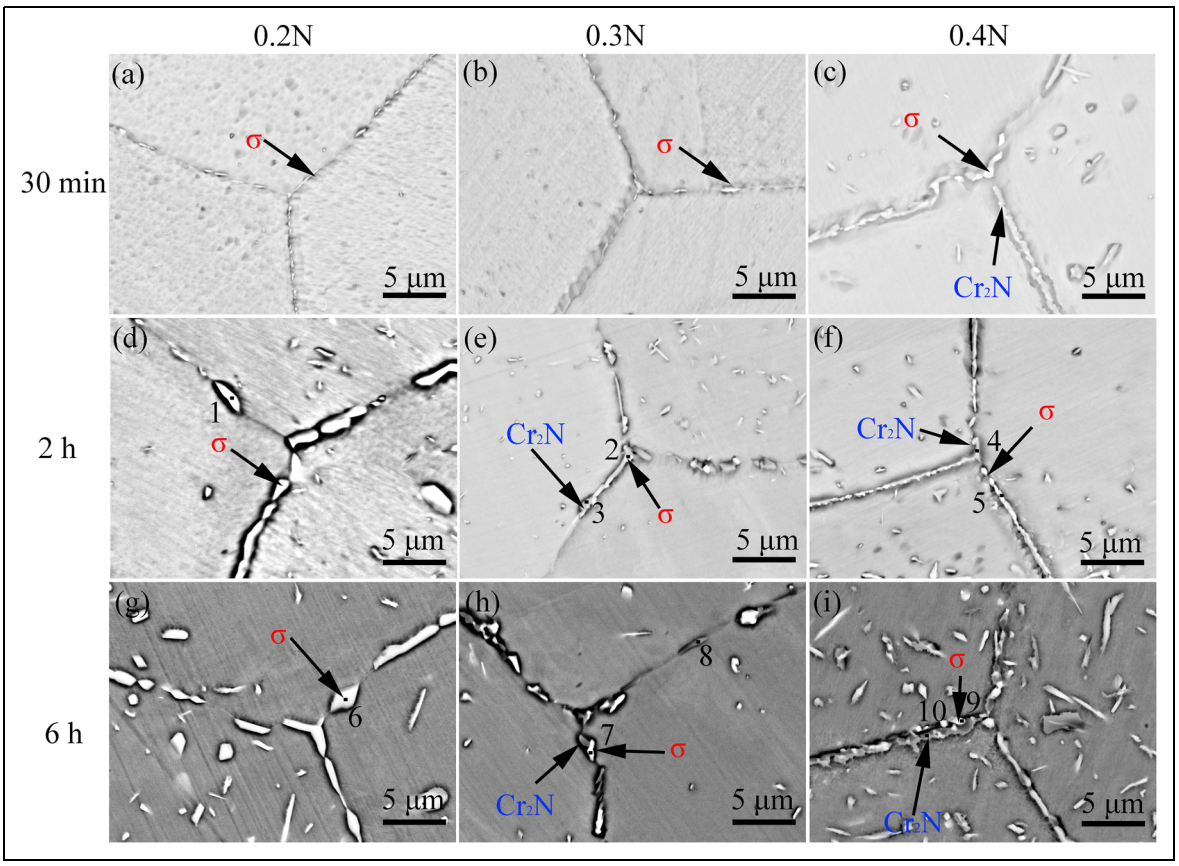

Figure 4. SEM-BSE images of the samples 0.2N, 0.3N and 0.4N aged at 950°C for 30 min ((a)–(c)), 2 h ((d)(f)) and 6 h ((g)–(i)). SEM: scanning electron microscope.

Table 2. Main compositions of the selected precipitates in grain boundary from SEM-EDS analysis.

Wt.%	Fe	Cr	Ni	Mo	C	N
No. 1	43.1	22.3	9.5	17.9	7.2	-
No. 2	41.9	17.2	12.7	16.7	11.4	-
No. 3	46.2	22.1	12.6	6.5	11.7	0.9
No. 4	35.4	18.0	16.3	22.7	7.6	-
No. 5	33.8	35.3	10.8	8.1	5.3	6.6
No. 6	42.8	19.7	11.5	18.3	7.7	-
No. 7	43.8	17.5	13.3	20.4	5.0	-
No. 8	33.7	39.1	10.4	6.1	5.1	5.6
No. 9	46.7	18.8	15.2	14.3	4.1	0.9
No. 10	40.1	32.0	12.8	5.9	4.1	5.1

EDS: energy-dispersive X-ray spectroscopy; SEM: scanning electron microscope.

about $a = b = 0.8799$ and $c = 0.4566$ nm, which is similar to the reported value.[8,40–42] However, the high-angle annular dark-field imaging in scanning transmission electron microscopy (HAADF-STEM) and STEM-Map (Figure 6(c) and (d)) also show the grain boundary with tiny amounts of Cr_2N phases besides more σ phases, and it is indicated that the σ phases was formed in Mo-rich, Fe-poor, Ni-poor zones, but the Cr and N segregations was observed after the emergence of Cr_2N phase. The precipitates shown in Figure 7(a) and Figure 8(a) can be confirmed as σ phases and Cr_2N phases based on the SAED and EDS shown in Figure 7(b) and (c) and Figure 8(b) and (c). The parameter of σ phase is the same as the phases shown in Figure 6(b), and the Cr_2N phases have the parameter is $a = b = 0.4811$ and $c = 0.4484$ nm, corresponding to the value in literature.[28,43] In addition, the HADDF-STEM and STEM-EDS Map displayed in Figure 7(d) and (e) and Figure 8(d) and (e) also suggested that the Mo segregation and Fe, Ni depletion had occurred along the grain boundary σ phase of 0.3N alloy, and Cr and N gather together near the Cr_2N phases. Further, the TEM and SAED also show the formation of σ and Cr_2N phases in 0.4N alloys, but most of the precipitates along the grain boundary are Cr_2N phases, based on the HADDF and EDS map analysis.

Electrochemical measurements

Polarisation curve measurements. Figure 9 shows the potentiodynamic polarisation curve of 6Mo SASS in 3.5% NaCl solution with pH = 1. There is a wide passivation area on each curve. After aging treatment, the current density of the passivation zone increases obviously, but the pitting potential (E_{pit}) does not change much. As can be seen from Figure 9(a), the passivation current density gradually increases with the increase of nitrogen content, because the alloy in solid solution does not have

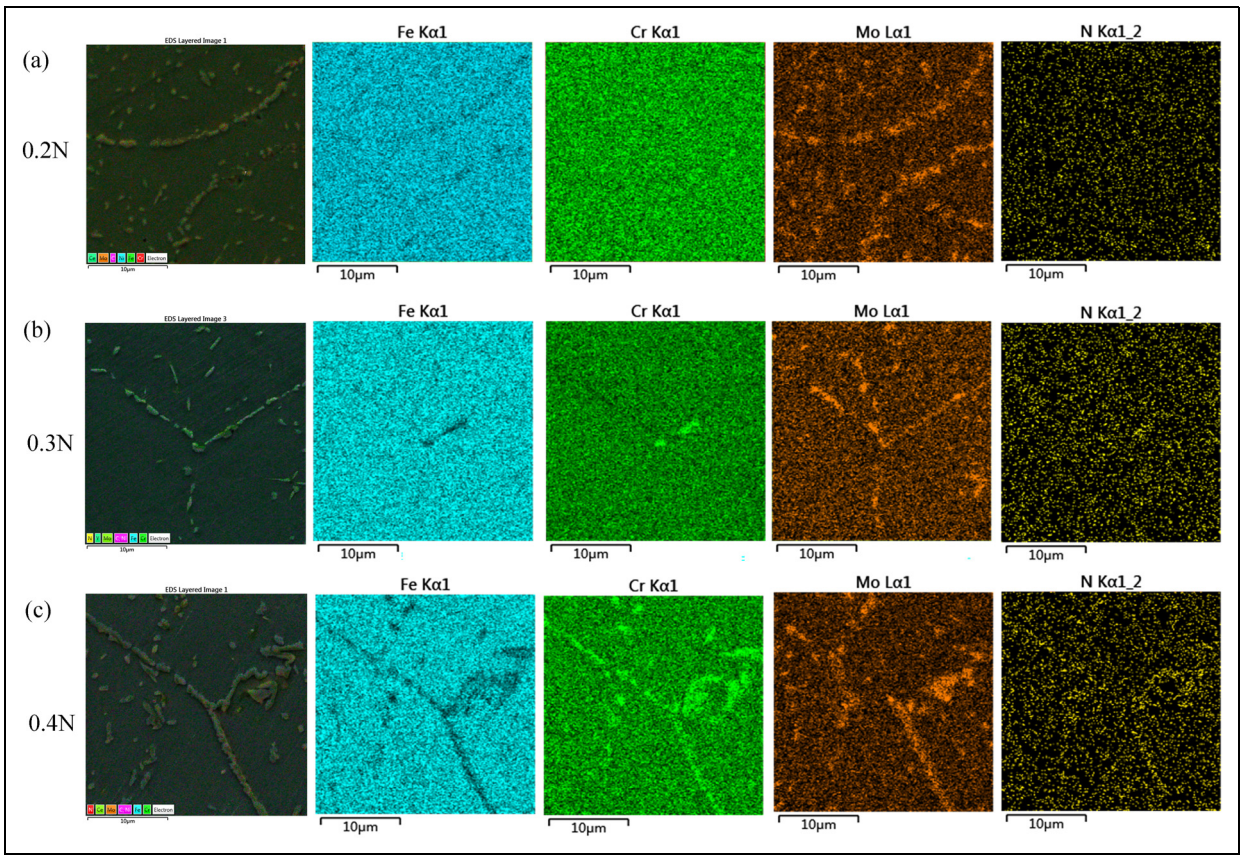

Figure 5. SEM-EDS mapping of the grain boundary precipitates in aged – 6 h 0.2N (a), 0.3N (b) and 0.4N (c) steels. EDS: energy-dispersive X-ray spectroscopy; SEM: scanning electron microscope.

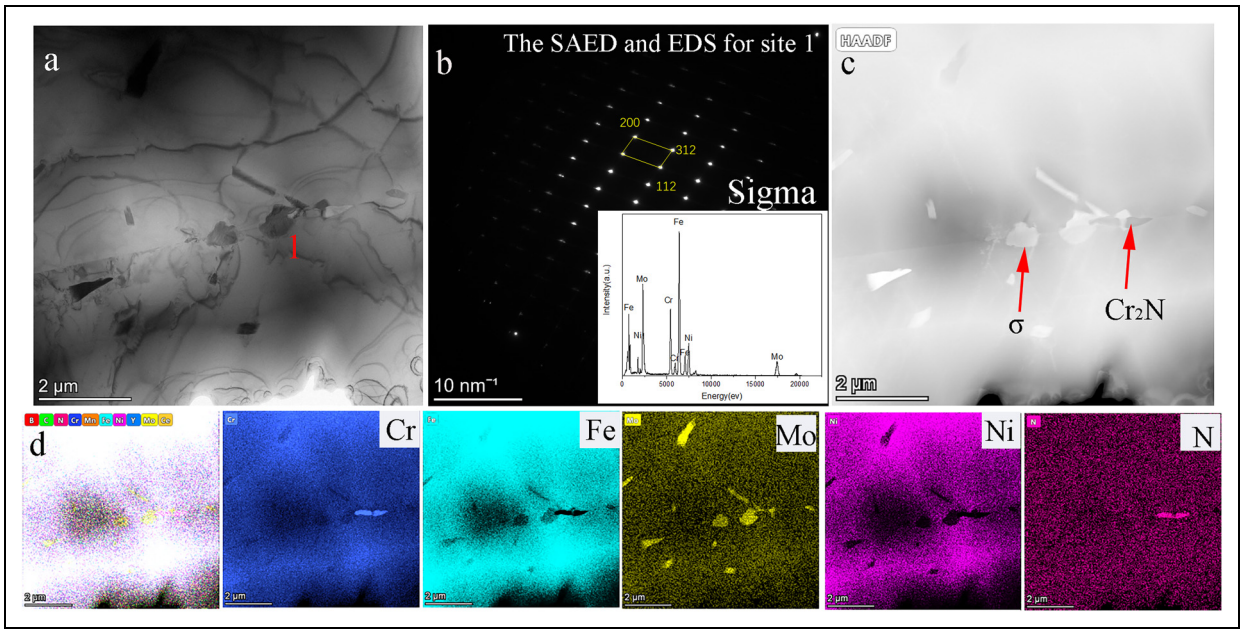

Figure 6. TEM (a), SAED (b), HAADF-STEM (c) and STEM-EDS maps (d) of grain boundary precipitates in the aged – 6 h 0.2N steels. EDS: energy-dispersive X-ray spectroscopy; SAED: selected area electron diffraction; TEM: transmission electron microscope; HAADF-STEM: high-angle annular dark-field imaging in scanning transmission electron microscopy.

any second phase precipitation, and 6Mo SASS with high nitrogen content has better passivation ability. However, after aging treatment at different times (as shown in Figure 9(a) to (c)), the alloy with medium nitrogen content has the lowest passivation current density, indicating that the passivation film of 0.3N

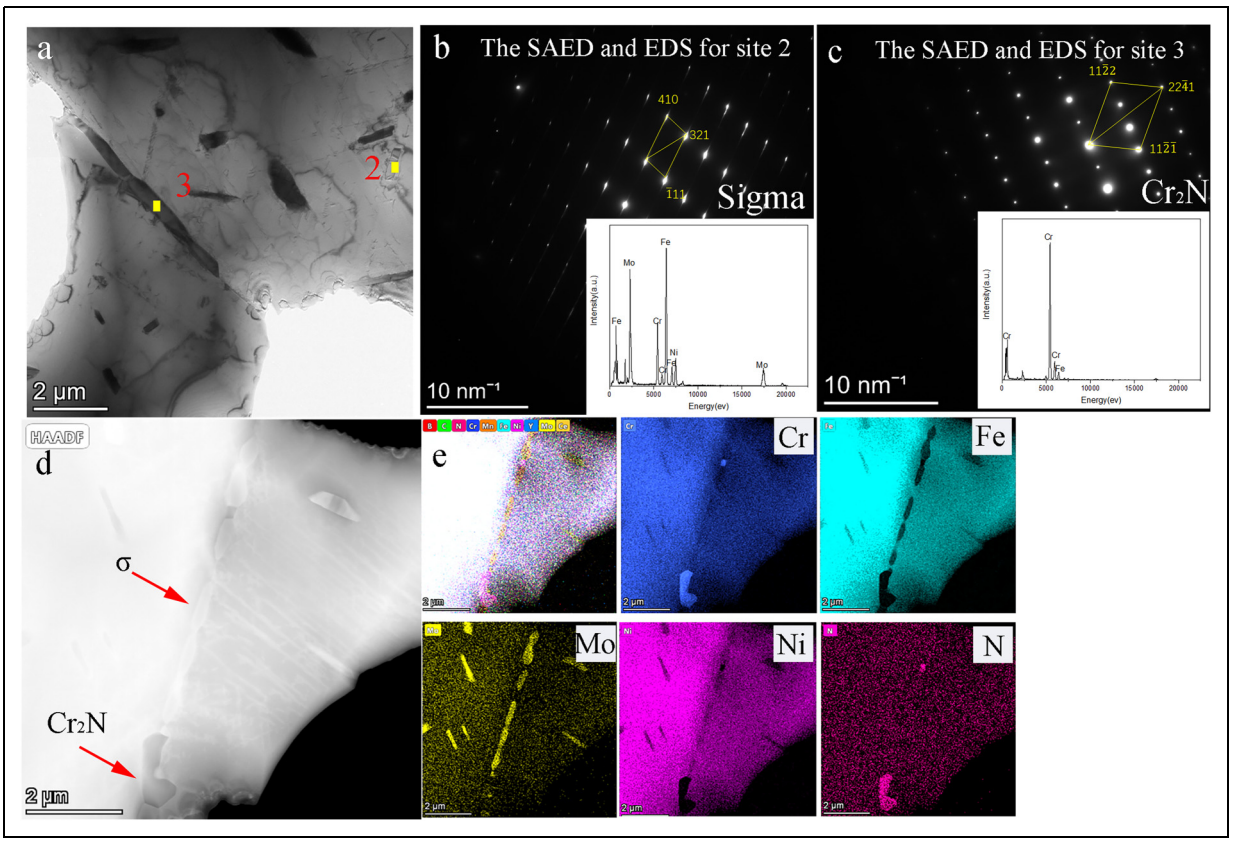

Figure 7. TEM (a), SAED (b),(c), HAADF-STEM (d) and STEM-EDS maps (e) of grain boundary precipitates in the aged – 6 h 0.3N steels. EDS: energy-dispersive X-ray spectroscopy; SAED: selected area electron diffraction; TEM: transmission electron microscope; HAADF-STEM: high-angle annular dark-field imaging in scanning transmission electron microscopy.

Table 3. Parameters of EIS of the test steels with different N contents in 3.5% NaCl solution with pH = 1.

Number	R_s/Ω	$Q_f/\times10^{-5}$ F	n	$R_f/\times10^{-4}$ Ω	$\sum\chi^2/\times10^{-4}$
0.2N-ST	18.46	5.949	0.9058	12.664	4.160
0.3N-ST	18.52	5.834	0.9059	13.744	4.993
0.4N-ST	18.68	5.646	0.9083	15.443	2.811
0.2N-30min	18.25	6.376	0.9025	9.214	5.924
0.3N-30min	18.35	5.936	0.9049	12.636	3.973
0.4N-30min	18.27	6.261	0.9109	9.736	2.320
0.2N-2h	18.10	6.657	0.9028	7.142	5.604
0.3N-2h	18.21	6.368	0.8924	9.252	7.144
0.4N-2h	17.61	7.144	0.8943	1.908	5.943
0.2N-6h	17.87	6.867	0.8929	4.086	6.694
0.3N-6h	18.13	6.576	0.9055	7.623	4.333
0.4N-6h	17.74	7.459	0.8941	0.990	6.033

alloy has the best protection ability, which is consistent with the results of precipitation behaviour observed by SEM.

Electrochemical impedance spectroscopy. Figure 10 shows the EIS experimental results of three alloys in 3.5% NaCl solution with pH = 1. It can be seen that the impedance mode value of each sample has little difference in the high-frequency region, which is related to the concentration stability of the system solution. However, in the low-frequency region, the impedance modulus decreases with the increase of aging time. Among the aging samples, the impedance modulus of 0.3N alloy is the largest. It can be seen that the Nyquist diagram of each sample presents a circular arc feature, and the radius of the circular arc is very different. For solid solution samples, the three alloys all have large arc, and the greater the nitrogen content and arc radius, the better the stability of passive film. After aging treatment, the arc radius decreases with the aging time, and the arc radius of 0.3N alloy is the largest among the three kinds of alloys.

To obtain the impedance parameters, the equivalent circuit shown in Figure 10(a) was used to fit the impedance data. Here, R_s represents the resistance of the electrolyte solution, while R_f represent the resistance of the passive film, respectively. The impedimetric data can be sufficiently modeled if instead of the capacitance of the passive film, the so-called constant phase element (CPE) is used. CPE value can be expressed as $1/(Q\ (j\omega)^n)$, so the total impedance value of the circuit can be expressed as:[19]

$$Z = R_s + \frac{1}{R_f + (j\omega)^{nQ}} \quad (1)$$

where Q_f is the CPE constant, ω is the angular frequency, j is the imaginary unit, and n is the CPE adjustment parameter. R_f represents the resistance during charge transfer,

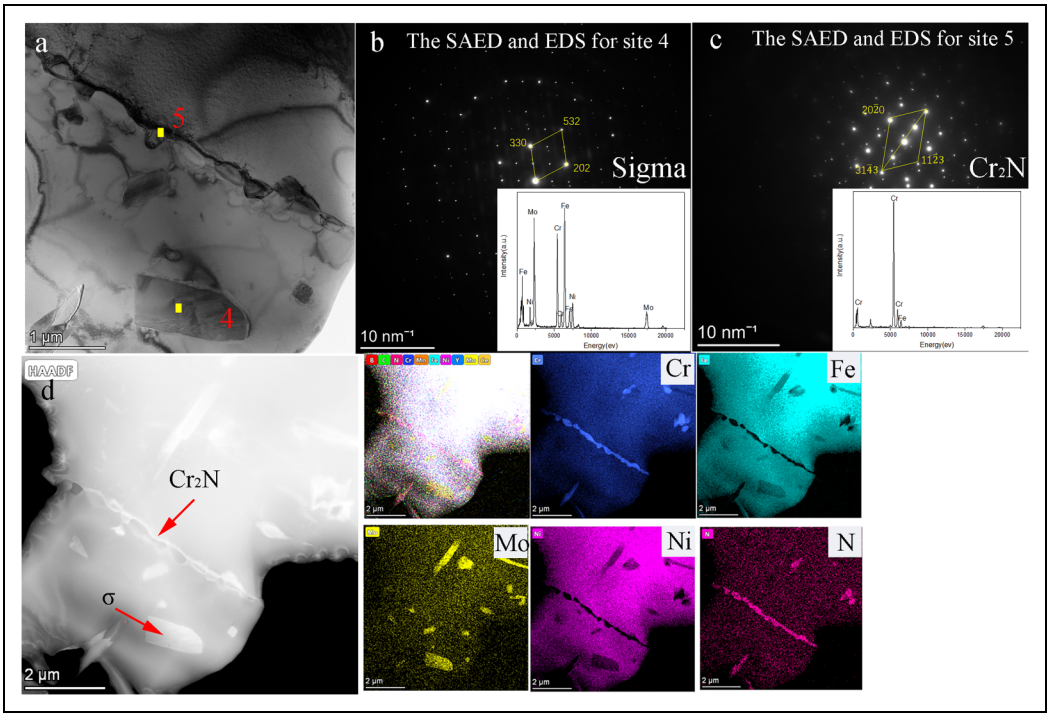

Figure 8. TEM (a), SAED (b), (c), HAADDF-STEM (d), and STEM-EDS maps (e) of grain boundary precipitates for the aged – 6 h 0.4N steels. EDS: energy-dispersive X-ray spectroscopy; SAED: selected area electron diffraction; TEM: transmission electron microscope; HAADF-STEM: high-angle annular dark-field imaging in scanning transmission electron microscopy.

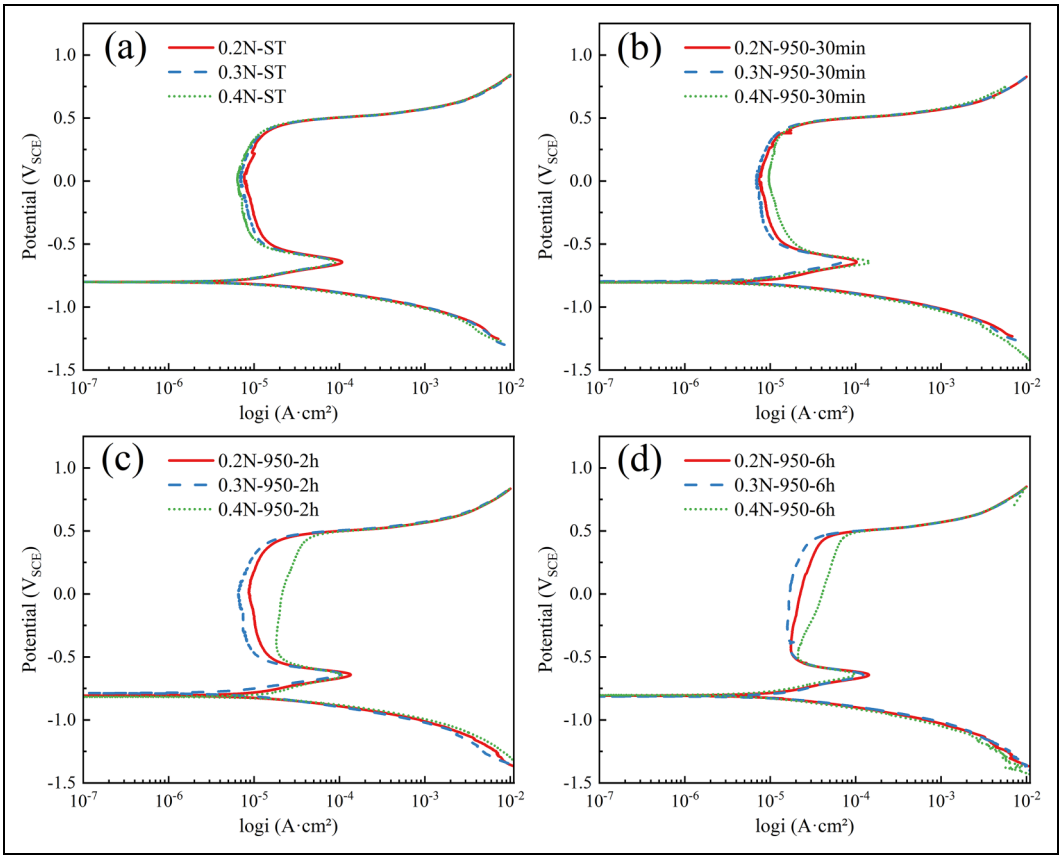

Figure 9. Potentiodynamic polarisation curve of 0.2N, 0.3N and 0.4N alloys. (a) solid–solution treatment, aged at 950°C for 30 min (b), 2 h (c) and 6 h (d).

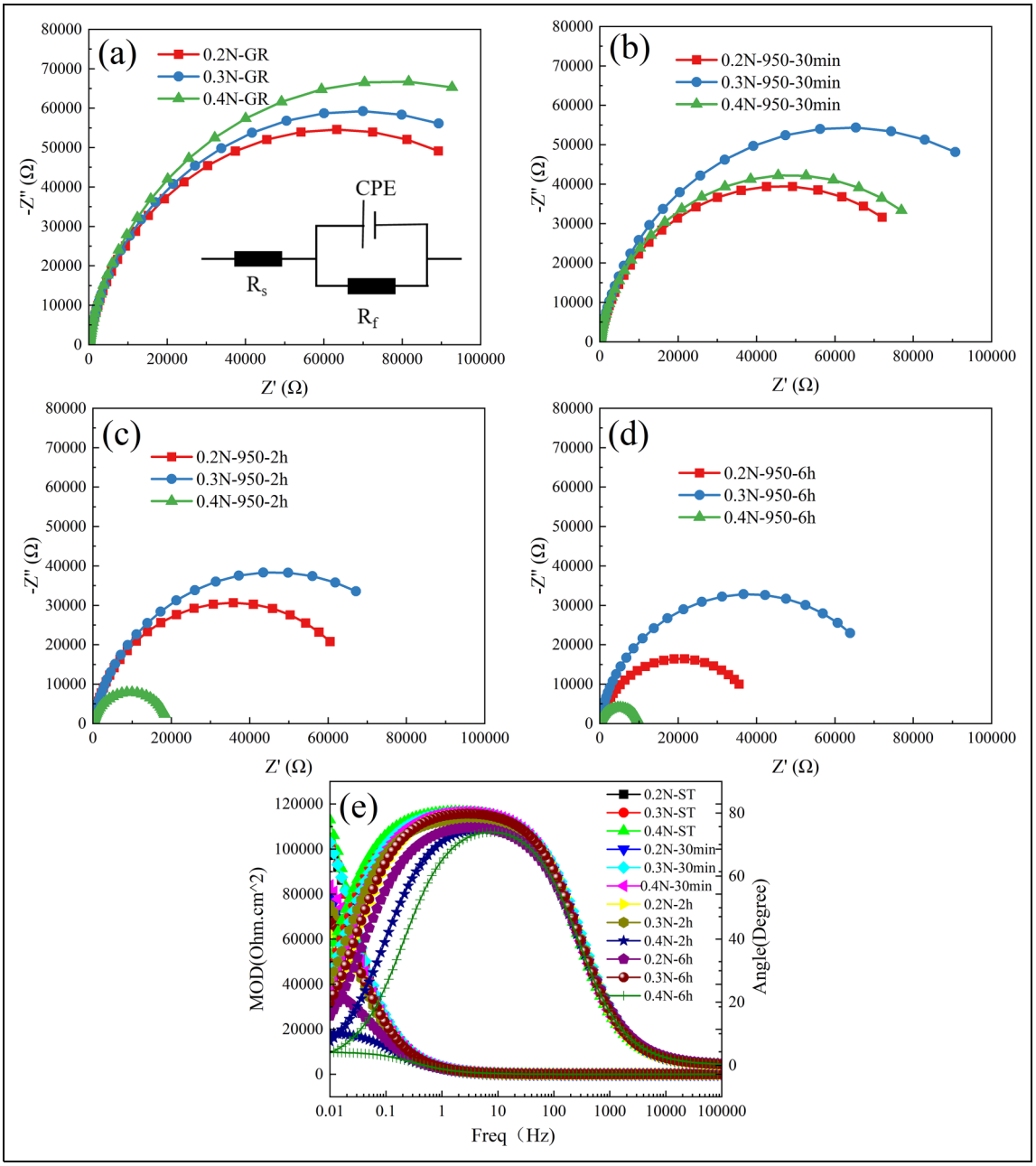

Figure 10. EIS of 0.2N, 0.3N and 0.4N alloys. Nyquist diagram of solid–solution treatment (a), aged at 950 °C for 30 min (b), 2 h (c) and 6 h (d), bode diagram of all samples (e). EIS: electrochemical impedance spectroscopy

and the larger the R_f, the more difficult the charge transfer and the better the corrosion resistance. The fitting results are shown in Table 3. It can be seen that among the alloys treated with the same aging time, the R_f of the passivation film of 0.3N alloy is the largest, indicating the best pitting resistance. In addition, The smaller the Q_f, the larger the CPE, which means there are fewer defects in the passivation film. Therefore, 0.3N alloy has the most stable passive film. These conclusions are consistent with the above-mentioned results of potentiodynamic polarisation.

DL-EPR curves. Figure 11 displays the DL-EPR curves of the 6Mo SASS with various N content after solid–solution and aging treatment. All the solution-annealing samples have no apparent reactivation current peak, indicating that these specimens have not suffered from the IGC. However, the aged samples in each material present noticeable activation current density peaks (I_a) and reactivation current density peaks (I_r). In addition, the peak intensity of I_r gradually increases with extending aging time, which suggests the DOS value would greatly rise. The DOS comparison of each steel aged at 950°C for the different aging periods was further shown in Figure 11(d). The 0.3N SASS exhibited the lowest DOS value at the same aging time among all the steels, due to the least precipitates along the grain boundary. Moreover, the DOS value in

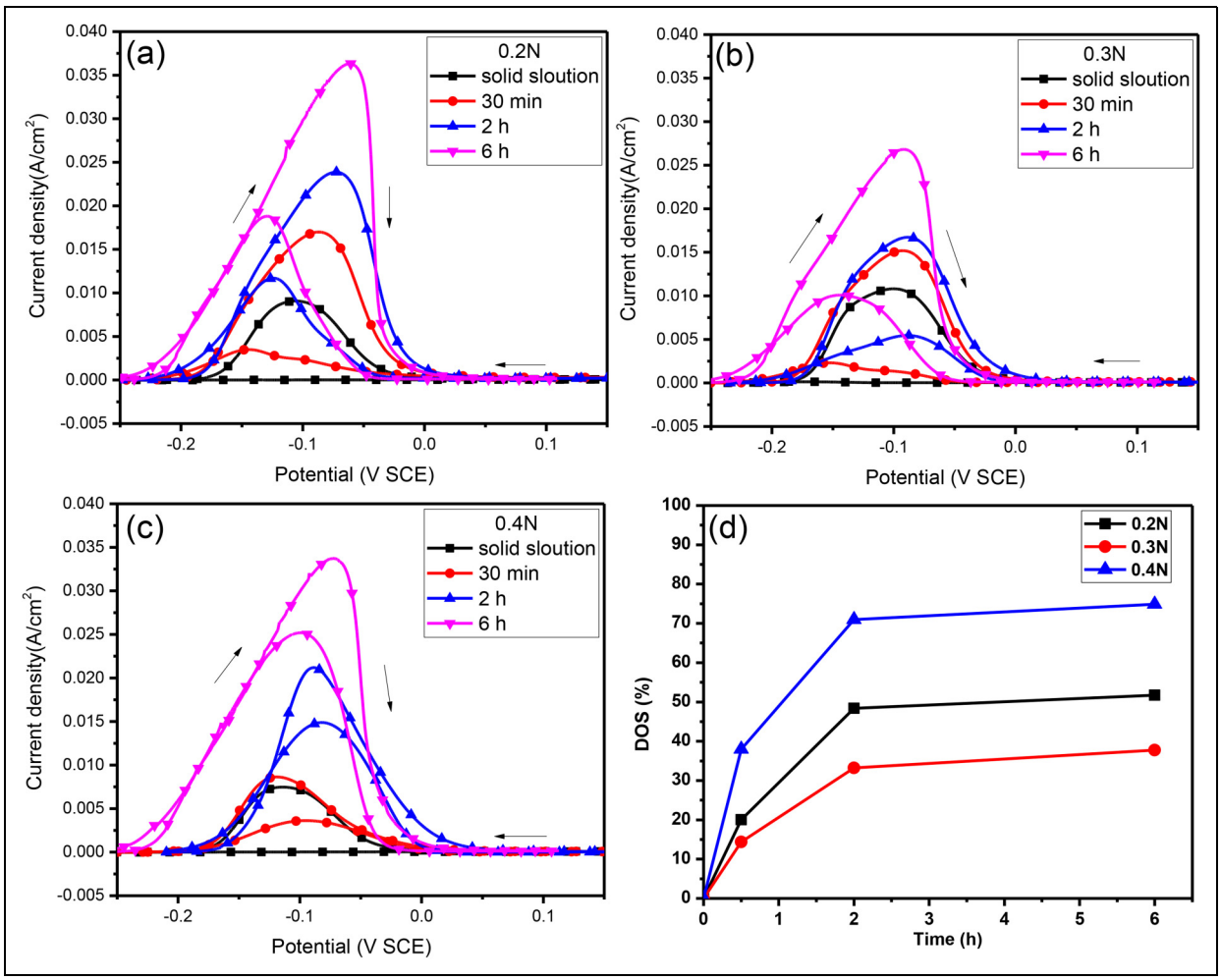

Figure 11. The DL-EPR curves of each steel at various aging times, (a) 0.2N, (b) 0.3N and (c) 0.4N; (d) the DOS comparison of each steel aged at 950°C at different aging times.

0.2N samples is much less than in 0.4N steels, corresponding to the grain boundary precipitation observation and calculation in Figure 3.

Effect mechanism of N on corrosion resistance

The equilibrium fraction of each phase in S31254 super stainless steels with different N content is shown in Figure 12. As shown in Figures 12(a) to (c), it can be observed that the Cr_2N and σ phases are almost stable in the range of about 500°C to 1200°C. The enlarged image for the equilibrium fraction of Cr_2N and σ phases was presented in Figure 12(d); the 0.4N alloy has an apparent less σ precipitate amounts than that of 0.2N and 0.3N alloy. However, some slightly more Cr_2N phases may be formed in 0.4N alloy in the temperature about from 900°C to 1200°C, compared to the other alloys. It has been confirmed that the increase of N content in S31654 SASS suppresses the precipitation of σ phases and promotes the formation of Cr_2N phases. The influence of N content on the aging precipitation of the as-examined samples is similar to the reported literature.[34] As the N addition increases, the amounts of σ phases gradually reduce, and the generation of Cr_2N phases is enhanced in the same aging period. Moreover, the 6Mo SASS with suitable N and Mn addition exhibited an efficient inhibition effect of phase precipitation along grain boundary since adding N and Mn is beneficial to stabilising the austenitic matrix. Therefore, the 0.3N has exhibited a much less precipitate amount of grain boundary phase than 0.2N and 0.4N specimens in the aging stage.

In order to further clarify the influence mechanism of N on the corrosion resistance of 6Mo SASS, the content distribution of each element was analysed by line scanning, and the results were shown in Figure 13. It can be seen that after 6 h aging treatment, Mo and Cr are obviously enriched at the grain boundary, and Fe content is decreased, indicating that precipitates rich in Mo and Cr are formed along the grain boundary, and the enrichment degree of 0.3N alloy is obviously smaller than that of the other two alloys. Moreover, the depleted areas of Mo and Cr can be obviously observed around the precipitates. In addition, we also found that N in 0.4N alloy is obviously enriched at the grain boundary, indicating that a large amount of Cr_2N phase is precipitated in 0.4N alloy, but not in 0.2N and 0.3N alloys.

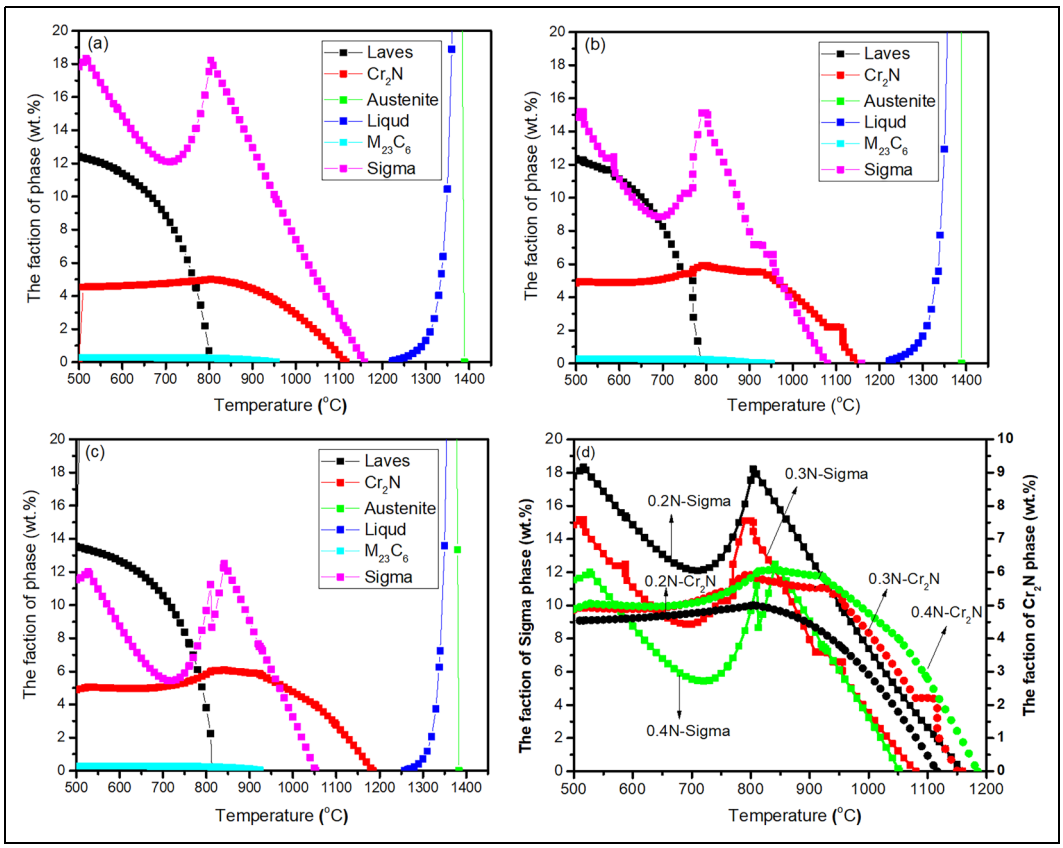

Figure 12. The equilibrium fraction of each phase in S31254 super stainless steels with different N content, (a) 0.2N, (b) 0.3N, (c) 0.4N; (d) the enlarged image for the equilibrium fraction of Cr_2N and sigma phase in three alloys.

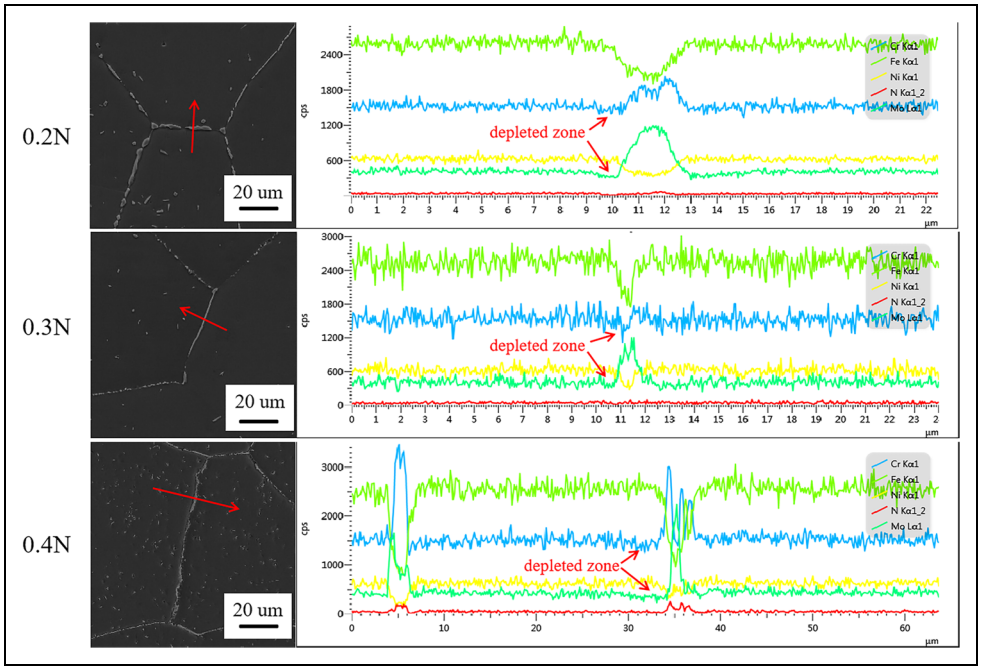

Figure 13. Line scanning results of 0.2N, 0.3N and 0.4N alloys after 6 h aging treatment.

As shown in Figure 4, with the increase of nitrogen content, the sediment area fraction decreases first and then increases, which means that the loss degree of Cr and Mo will also decrease first and then increase, which is confirmed by the line scanning results in Figure 13. As we all know, Cr and Mo are the main elements in the formation

of 6Mo SASS passive film, and the depletion of Cr and Mo will lead to a serious reduction in the continuity and density of the passive film. The dilution degree of 0.3N alloy around the precipitation phase is relatively small, and the passivation film formed on the surface of stainless steel is more stable and has better pitting resistance. In addition, the IGC degree of stainless steel mainly depends on the degree of Cr and Mo depletion zone at grain boundaries, and the degree of depletion is closely related to the total amount of sediment.[34] The 0.3N alloy can well inhibit the precipitation behaviour of grain boundary phase, reduce the total precipitated phase of the alloy, thus reducing the depletion range and improving the IGC resistance.

Conclusions

The 6Mo SASS with nitrogen contents of 0.20, 0.28 and 0.38 wt.% was melted while maintaining a relatively high manganese level of about 1.5 wt.% and nickel content of around 18 wt.%. The samples were labelled as 0.2N, 0.3N, and 0.4N, and the effects of nitrogen content on the micro-structure and corrosion resistance of 6Mo SASS were examined. The size and total amount of the precipitated phase increase with aging time. As nitrogen content increases, the segregation of molybdenum in 6Mo SASS decreases, which helps to prevent the formation of the σ phase. However, nitrogen segregation at the grain boundaries increases, facilitating the formation of the Cr_2N phase. As a result, the area fraction of the precipitated phase in the 0.3N alloy is significantly lower than in the other two samples after the same aging period. For the solid solution sample, the alloy's resistance to pitting improves with higher nitrogen content. In samples that underwent aging treatment, the 0.3N exhibited a significantly lower amount of grain boundary precipitate compared to the 0.2N and 0.4N specimens during the aging process, giving the 0.3N SASS the best corrosion resistance at the same aging duration.

Authorship

JW was involved in investigation, methodology, data curation, formal analysis and writing – original-draft. YY and ZL were involved in data curation and formal analysis. HT and CC were involved in validation and writing – review & editing. LC was involved in writing – review & editing. YG-G was involved in supervision and writing – review & editing. PH was involved in supervision, writing – review & editing and funding acquisition.

Declaration of conflicting interests

The authors declared no potential conflicts of interest with respect to the research, authorship, and/or publication of this article.

Funding

The authors disclosed receipt of the following financial support for the research, authorship, and/or publication of this article: The present work was financially supported by the National Natural Science Foundation of China (52104338), Shanxi Province Science and Technology Cooperation and Exchange Special Project (202304041101015) and Applied Fundamental Research Programs of Shanxi Province (202303021221036).

ORCID iDs

Haiyu Tian https://orcid.org/0009-0000-3746-4501
Chao Chen https://orcid.org/0000-0001-7953-1127

References

1. Zhang JN, Hu WP, Cao S, et al. Recent progress for hydrogen production by photocatalytic natural or simulated seawater splitting. *Nano Res* 2020; 13: 2313–2322.
2. Chen TT, Wang J, Zhang Y, et al. Twin density gradient induces enhanced yield strength-and-ductility synergy in a S31254 super austenitic stainless steel. *Mater Sci Eng A* 2022; 837: 142727.
3. Yu JT, Zhang SC, Li HB, et al. Influence mechanism of boron segregation on the microstructure evolution and hot ductility of super austenitic stainless steel S32654. *J Mater Sci Technol* 2022; 112: 184–194.
4. Grubb JF, Polinski RE, Fritz JD, et al. A 6% Mo stainless steel for flue gas desulfurization. In: Corrosion 2000, 2000. Orlando: NACE International.
5. Wang JX, Shi W, Xiang S, et al. Study of the corrosion behaviour of sensitized 904L austenitic stainless steel in Cl-solution. *Corros Sci* 2021; 181: 109234.
6. Sunny KT and Korra NN. A systematic review about welding of super austenitic stainless steel. *Mater Today: Proc* 2021; 47: 4378–4381.
7. Marin R, Combeau H, Zollinger J, et al. σ-Phase formation in super austenitic stainless steel during directional solidification and subsequent phase transformations. *Metall Mater Trans A* 2020; 51: 3526–3534.
8. Hao YS, Liu WC, Li J, et al. Microstructural bandings evolution behavior and their effects on microstructure and mechanical property of super-austenitic stainless steel. *Mater Sci Eng A* 2018; 736: 258–268.
9. Phillips NSL, Chumbley LS and Gleeson B. Phase transformations in cast superaustenitic stainless steels. *J Mater Eng Perform* 2009; 18: 1285–1293.
10. Gao Q, Ding Z and Liao WH. Effective elastic properties of irregular auxetic structures. *Compos Struct* 2022; 287: 115269.
11. Li YT, Chen XM, Zeng XK, et al. Hard yet tough and self-lubricating $(CuNiTiNbCr)C_x$ high-entropy nanocomposite films: effects of carbon content on structure and properties. *J Mater Sci Technol* 2024; 173: 20–30.
12. Yang Z, Chen C, Li D, et al. An additively manufactured heat-resistant Al-Ce-Sc-Zr alloy: microstructure, mechanical properties and thermal stability. *Mater Sci EngA* 2023; 872: 144965.
13. Wang S, Chen X, Luo K, et al. The design of low-temperature solder alloys and the comparison of mechanical performance of solder joints on ENIG and ENEPIG interface. *J Mater Res Technol* 2023; 27: 5332–5339.
14. Zhang SC, Jiang HB, Zhang BB, et al. Effects of Cr and Mo on precipitation behavior and associated intergranular corrosion susceptibility of superaustenitic stainless steel S32654. *Mater Charact* 2019; 152: 141–150.

15. Liao LH, Li JY, Zhao ZX, et al. Precipitation and phase transformation behavior during high-temperature aging of a cobalt modified Fe-24Cr-(22-x)Ni-7Mo-xCo superaustenitic stainless steel. *J Mater Sci* 2022; 57: 4771–4788.
16. Wang Q, Wang LJ, Sun YH, et al. The influence of Ce microalloying on the precipitation of intermetallic sigma phase during solidification of super-austenitic stainless steels. *J Alloys Compd* 2020; 815: 152418.
17. Zhang SC, Yu JT, Li HB, et al. Refinement mechanism of cerium addition on solidification structure and sigma phase of super austenitic stainless steel S32654. *J Mater Sci Technol* 2022; 102: 105–114.
18. Zhang X, Zhi J, Song X, et al. Impact of cerium on microstructure of rust and corrosion resistance of Cu-Cr-Ni-V micro-alloyed steels in $NaHSO_3$ acid accelerated test. *Ironmak Steelmak* 2024. doi:10.1177/03019233241254662
19. Zhang X, Zhi J, Song X, et al. Influence of cerium on impact toughness, tensile properties and inclusion of industrial Al-killed steel Q355B. *J Mater Res Technol* 2024; 32: 1118–1126.
20. Sanhueza JP, Montoya LF, Toledo E, et al. Design and characterization of super austenitic stainless steel stabilized with niobium produced by induction melting at open atmosphere. *Steel Res Int* 2018; 89: 1800215.
21. Li BB, Qu HP, Lang YP, et al. Copper alloying content effect on pitting resistance of modified 00Cr20Ni18Mo6CuN super austenitic stainless steels. *Corros Sci* 2020; 173: 108791.
22. Bai JG, Cui YS, Wang J, et al. Effect of compression deformation on precipitation phase behavior of B-containing S31254 super austenitic stainless steel. *J Iron Steel Res Int* 2019; 26: 712–719.
23. Wang J, Cui YS, Bai JG, et al. The mechanism on the B addition to regulate phase precipitation and improve intergranular corrosion resistance in UNS S31254 superaustenitic stainless steels. *J Electrochem Soc* 2019; 166: C600.
24. Simmons JW. Overview: high-nitrogen alloying of stainless steels. *Sci Eng A* 1996; 207: 159–169.
25. Reed RP. Nitrogen in austenitic stainless steels. *JOM* 1989; 41: 16–21.
26. Li S, Zhang CS, Lu JP, et al. A review of progress on high nitrogen austenitic stainless-steel research. *Mater Express* 2021; 11: 1901–1925.
27. Lang YP, Qu HP, Chen HT, et al. Research progress and development tendency of nitrogen-alloyed austenitic stainless steels. *J Iron Steel Res Int* 2015; 22: 91–98.
28. Lee TH, Kim SJ and Jung YC. Crystallographic details of precipitates in Fe-22Cr-21Ni-6Mo-(N) superaustenitic stainless steels aged at 900°C. *Metall Mater Trans A* 2000; 31: 1713–1723.
29. Ma XP, Wang LJ, Qin B, et al. Effect of N on microstructure and mechanical properties of 16Cr5Ni1Mo martensitic stainless steel. *Mater Des* 2012; 34: 74–81.
30. Mudali UK. Nitrogen-a boon to the metals industry. *Mater Manuf Processes* 2004; 19: 1–5.
31. Rajendran N and Rajeswari S. Super austenitic stainless steels-a promising replacement for the currently used type 316L stainless steel as the construction material for flue-gas desulphurization plant. *J Mater Sci* 1996; 31: 6615–6619.
32. Behrens R, Alves H and Stenner F. New developed 6-Mo super-austenitic stainless steel with low sigma solvus temperature and high resistance to localized corrosion. In: Corrosion 2013, 2013. Orlando: NACE International.
33. Chandrasekar A, Anburaj J, Narayanan R, et al. Solubility of nitrogen in superaustenitic stainless steels during air induction melting. *J Mater Eng Perform* 2013; 22: 964–973.
34. Zhang SC, Li HB, Jiang ZH, et al. Influence of N on precipitation behavior, associated corrosion and mechanical properties of super austenitic stainless steel S32654. *J Mater Sci Technol* 2020; 42: 143–155.
35. Sun L, Sun YT, Lv CX, et al. Studies on the degree of sensitization of hyper-duplex stainless steel 2707 at 900°C using a modified DL-EPR test. *Corros Sci* 2021; 185: 109432.
36. Li JC, Li GP, Liang W, et al. Effect of aging on precipitation behavior and pitting corrosion resistance of SAF2906 super duplex stainless steel. *J Mater Eng Perform* 2017; 26: 4533–4543.
37. Zhao H, Zhang ZY, Zhang HZ, et al. Effect of aging time on intergranular corrosion behavior of a newly developed LDX 2404 lean duplex stainless steel. *J Alloys Compd* 2016; 672: 147–154.
38. Lee C, Lee Y, Lee C, et al. Precipitation behavior of the sigma phase with Ni and Mn content variations in superaustenitic stainless steel weld metal. *Mater Charact* 2018; 144: 148–154.
39. Heino S. Role of Mo and W during sensitization of superaustenitic stainless steel-crystallography and composition of precipitates. *Metall Mater Trans A* 2000; 31: 1893–1905.
40. Koutsoukis T, Redjaïmia A and Fourlaris G. Phase transformations and mechanical properties in heat treated superaustenitic stainless steels. *Mater Sci Eng A* 2013; 561: 477–485.
41. Anburaj J, Mohamed Nazirudeen SS, Narayanan R, et al. Ageing of forged superaustenitic stainless steel: precipitate phases and mechanical properties. *Mater Sci Eng A* 2012; 535: 99–107.
42. Zhang SC, Jiang ZH, Li HB, et al. Precipitation behavior and phase transformation mechanism of super austenitic stainless steel S32654 during isothermal aging. *Mater Charact* 2018; 137: 244–255.
43. Zhang SC, Jiang ZH, Li HB, et al. Detection of susceptibility to intergranular corrosion of aged super austenitic stainless steel S32654 by a modified electrochemical potentiokinetic reactivation method. *J Alloys Compd* 2017; 695: 3083–3093.